Polymorphic Phases of Metal Chlorides in the Confined 2D Space of Bilayer Graphene

Lin, Y.-C.; Motoyama, A.; Kretschmer, S.; Ghaderzadeh, S.; Ghorbani Asl, M.; Araki, Y.; Krasheninnikov, A.; Ago, H.; Suenaga, K.;

Originally published:

December 2021

Advanced Materials 33(2021), 2105898

DOI: https://doi.org/10.1002/adma.202105898

Polymorphic phases of metal chlorides in the confined 2D space of bilayer graphene

Yung-Chang Lin[1]*, Amane Motoyama[2], Silvan Kretschmer[3], Sadegh Ghaderzadeh[3], Mahdi Ghorbani-Asl[3], Yuji Araki[2], Arkady V. Krasheninnikov[3,4], Hiroki Ago[2,5], Kazu Suenaga[1,6]*

[1]Nanomaterials Research Institute, National Institute of Advanced Industrial Science and Technology (AIST), Tsukuba 305-8565, Japan

[2]Interdisciplinary Graduate School of Engineering Sciences, Kyushu University, Fukuoka 816-8580, Japan

[3]Institute of Ion Beam Physics and Materials Research, Helmholtz-Zentrum Dresden-Rossendorf, 01328 Dresden, Germany

[4]Department of Applied Physics, Aalto University, P.O. Box 11100, 00076 Aalto, Finland

[5]Global Innovation Center (GIC), Kyushu University, Fukuoka 816-8580, Japan

[6]The Institute of Scientific and Industrial Research (ISIR-SANKEN), Osaka University, Osaka 567-0047, Japan

Abstract

Unprecedented two-dimensional (2D) metal chloride structures were grown between sheets of bilayer graphene through intercalation of metal and chlorine atoms. Numerous spatially confined 2D phases of $AlCl_3$ and $CuCl_2$ distinct from their typical bulk forms were found, and the transformations between these new phases under the electron beam were directly observed by *in situ* scanning transmission electron microscopy (STEM). Our density functional theory calculations confirmed the metastability of the atomic structures derived from the STEM experiments and provided insights into the electronic properties of the phases, which range from insulators to semimetals. Additionally, the co-intercalation of different metal chlorides was found to create completely new hybrid systems; in-plane quasi-1D $AlCl_3/CuCl_2$ heterostructures were obtained. The existence of polymorphic phases hints at the unique possibilities for fabricating new types of 2D materials with diverse electronic properties confined between graphene sheets.

Keywords: graphene intercalation, STEM, EELS, metal chloride, phase transition

Corresponding authors: yc-lin@aist.go.jp, suenaga-kazu@sanken.osaka-u.ac.jp

Low-dimensional materials have attracted considerable research interest because of their intriguing properties as well as their integration-based flexibility for fabricating unconventional heterogeneous structures[1]. Growth and transfer techniques[2,3] have been employed to design planar[4–7], vertical[8], and even core–shell[9] complex materials with unique characteristics such as ultra-high mobility, electronic properties dependent on atomic reconstructions induced by the inter-layer interaction[10], superconductivity[11], magnetism[12,13], strain-engineered luminescence[14], and angle-dependent excitonic/plasmonic[15] properties that are distinct from those of their isolated components. Additionally, new classes of low-dimensional composites can be realized by loading materials into the tubular space of nanotubes[16] or the van der Waals (vdW) gaps of layered materials[17], and the physical and chemical properties of the host materials are known to be drastically altered by the intercalants[18–20].

The planar carbon allotrope, graphite, which features robust in-plane covalent bonding and weak vdW interactions between adjacent layers, is the most widely studied material in the context of intercalation. Extensive investigations on the intercalation chemistry of graphite since the 1920s[21–23] have laid the foundation for the development of rechargeable metal-ion (Li, Na, K) batteries[24,25], and hinted at the possibility of realizing superconductivity in K, Ca, and Yb-intercalated graphitic compounds [26–29]. For the metal chloride intercalation, $FeCl_3$ have shown great potential in transparent electrodes[30,31] with unique magnetic properties[12,13], while $AlCl_3$ have been reported as a low-cost, high-capacity ultrafast rechargeable battery with low flammability[32,33]. This

compound is believed to switch between $AlCl_4^-$ monomers and $Al_2Cl_7^-$ dimers during the charge and discharge states. The phase transformations of metal chlorides are expected to occur within the vdW gap in graphite and bilayer graphene (BLG), but it has never been directly observed.

At the same time, chemically inert and mechanically robust graphene sheets can assist in not only stabilizing the intercalated compounds, but also in getting insight into their structure and properties. Thanks to the recent developments in transmission electron microscopy, obtaining the atomic-resolution images of the intercalants inside the graphene layers became recently possible[34,35]. As the intercalation chemistry in BLG and in graphite is still not fully understood yet, the STEM data may be extremely useful in that context.

Here, using state-of-the art STEM, we study the intercalation of metal and Cl atoms into BLG and demonstrate the possibility of using gaps in BLG to grow new 2D materials. We observe formations of new 2D phases of $AlCl_3$ and $CuCl_2$, as well as the transformations between the phases, and appearance of alloy structures. By combining the experiments with first-principles calculations, we further get insight into the properties of these novel materials.

A large-area (~5 × 5 cm^2) and uniform BLG grown on a Cu-Ni alloy catalyst by chemical vapor deposition (CVD)[36,37] was employed for growing 2D materials in the vdW gaps (Fig. 1a). The as-grown BLG was transferred to a TEM grid, which was subsequently placed in a vacuum-sealed glass tube to facilitate metal chloride ($AlCl_3$ and $CuCl_2$) intercalation via chemical vapor transport[38]. Generally, bulk metal chlorides have the chemical formula MCl_x, where each metal (M) atom is coordinated with six chlorine

(Cl) atoms in an octahedral geometry; however, the compounds have distinct crystal structures depending on the stoichiometric amount of Cl. The ideal atomic structures of single-layer MCl_x compounds (x = 2–5) expected from the bulk system are shown in Fig. 1b-1e; more than 40 types of metal chlorides have been reported in studies on graphite intercalation compounds (GICs)[39].

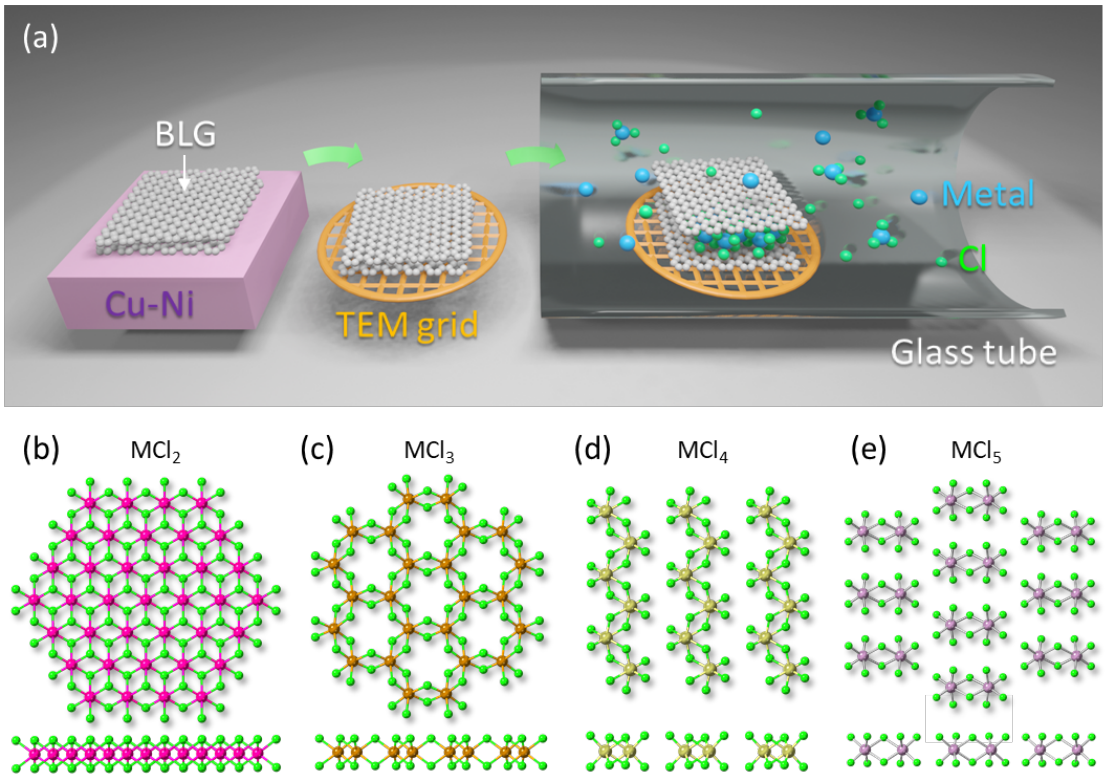

Fig. 1. Metal chloride intercalation in bilayer graphene (BLG). (a) Schematic of the steps involved in the intercalation of metal chlorides into BLG. Ideal atomic models of single-layer metal chlorides MCl_2 (b), MCl_3 (c), MCl_4 (d), and MCl_5 (e). Both MCl_2 and MCl_3 are octahedral layered crystals, where the metal atoms occupy a hexagonally closet-packed lattice plane in MCl_2, but the MCl_3 possess one-third of the octahedral vacancies at the M sites. The MCl_4 is a layered monoclinic crystal consisting of infinite edge-shared zigzag octahedral chains, while the MCl_5 is dimerized and features an orthorhombic crystal.

Studies on nanotube encapsulation have indicated that the structure of the materials inside nanotubes can be completely different from their 3D forms because of spatial confinement[40–42]. Indeed, in addition to the 'conventional' phase known from bulk $AlCl_3$, of the 2D-$AlCl_3$ (*n*-$AlCl_3$, Fig. S1a), we observed several new polymorphic phases of AlCl3 intercalated in BLG ($AlCl_3$@BLG). Specifically, three previously unknown new 2D-$AlCl_3$ structures (Fig. 2a–2c) were found. The three phases of $AlCl_3$ emerged simultaneously at the same growth condition. Their atomic structures were determined by density functional theory (DFT) calculations using experimentally obtained images as inputs.

The first new $AlCl_3$ phase represents a trimerized form of an Al_3Cl_9 cluster (denoted as α-$AlCl_3$ herein) where the $AlCl_3$ molecules are stabilized in a circular arrangement, as shown in Fig. 2a. The corresponding atomic model is presented in Fig. 2d. The second unique 2D-$AlCl_3$ structure exhibits orthorhombic symmetry (denoted as β-$AlCl_3$), with arrays of "eye-mask" icositetragons (24-sided polygons) surrounded by rhombus-shaped octagons, as shown in Fig. 2b; the corresponding atomic structure is depicted in Fig. 2e. The ADF contrast of the two isolated $AlCl_3$ units in the eye-mask-shaped icositetragon is presumably a superposition of two translational swap configurations, as shown in Fig. S2. The third new 2D-$AlCl_3$ phase (γ-$AlCl_3$) has a ladder-like structure, as shown in Fig. 2c. The γ-$AlCl_3$ polymorph exhibits orthogonal symmetry and consists of parallel rows of hexadecagons separated by parallel rows of rhombus-shaped octagons, as shown in the corresponding atomic model in Fig. 2f. The α-, β-, and γ-$AlCl_3$ structures are completely different from each other and also distinct from the *n*-$AlCl_3$, as evident from by the

detailed comparison of their crystallinities presented in Fig. S1. *n*-$AlCl_3$ and the three new phases (α-, β-, γ-$AlCl_3$) are different in terms of the bonding configuration. An Al atom in the *n*-$AlCl_3$ phase is bonded to six Cl atoms, whereas the coordination number of Al is three in the α-phase and four in the β- and γ-$AlCl_3$ phases. EELS fine structure analysis indicates that the Al *L*-edge reflects the nearest-neighbor bonding characteristics or its coordination numbers[43]. Figure S3 suggests that the Al *L*-edge of the α-, β-, and γ-$AlCl_3$ phases exhibits similar features, with an intense peak at 76.0 eV and another lower-intensity peak at 77.3 eV, indicating similar three-bond and four-bond Al configurations. However, the *n*-$AlCl_3$ phase with six-bond Al exhibits red shift of the first intense peak (75.6 eV) and does not feature a second peak in the Al *L*-edge. Quantitative contrast comparison between the experimental and simulated ADF images are presented in Fig. S4. The thickness of the polymorphic phases of $AlCl_3$ intercalation in BLG is quantitively estimated by Fourier-log analysis. The log-ratio formula is expressed as $t/\lambda^* = \ln(I_t/I_0)$ where t is the specimen thickness, λ^* is the local inelastic mean free path, I_0 is the zero-loss intensity, and I_t is the total transmitted intensity under the EELS[44]. Here, we list the t/λ^* of vacuum = 0, BLG = 0.04, *n*-$AlCl_3$, α-$AlCl_3$, β-$AlCl_3$, and γ-$AlCl_3$ = 0.06 (see more details in Table S1).

Charge transfer is expected to occur during the intercalation of BLG. The calculated charge transfer from BLG to the α-$AlCl_3$, β-$AlCl_3$, and γ-$AlCl_3$ phases is depicted in the charge density difference plots shown in Fig. 2g–2i, respectively. Based on the electron excess (yellow areas) and depletion (cyan areas) plot, the redistribution of the electronic charge upon intercalation is complex, and as the intercalated structures are not symmetric, the gain/loss for the graphene sheets can be different. Overall, electrons appear to be transferred to the α-$AlCl_3$ and β-$AlCl_3$ layers, and the opposite is true for the γ-$AlCl_3$

layers, see Table S2.

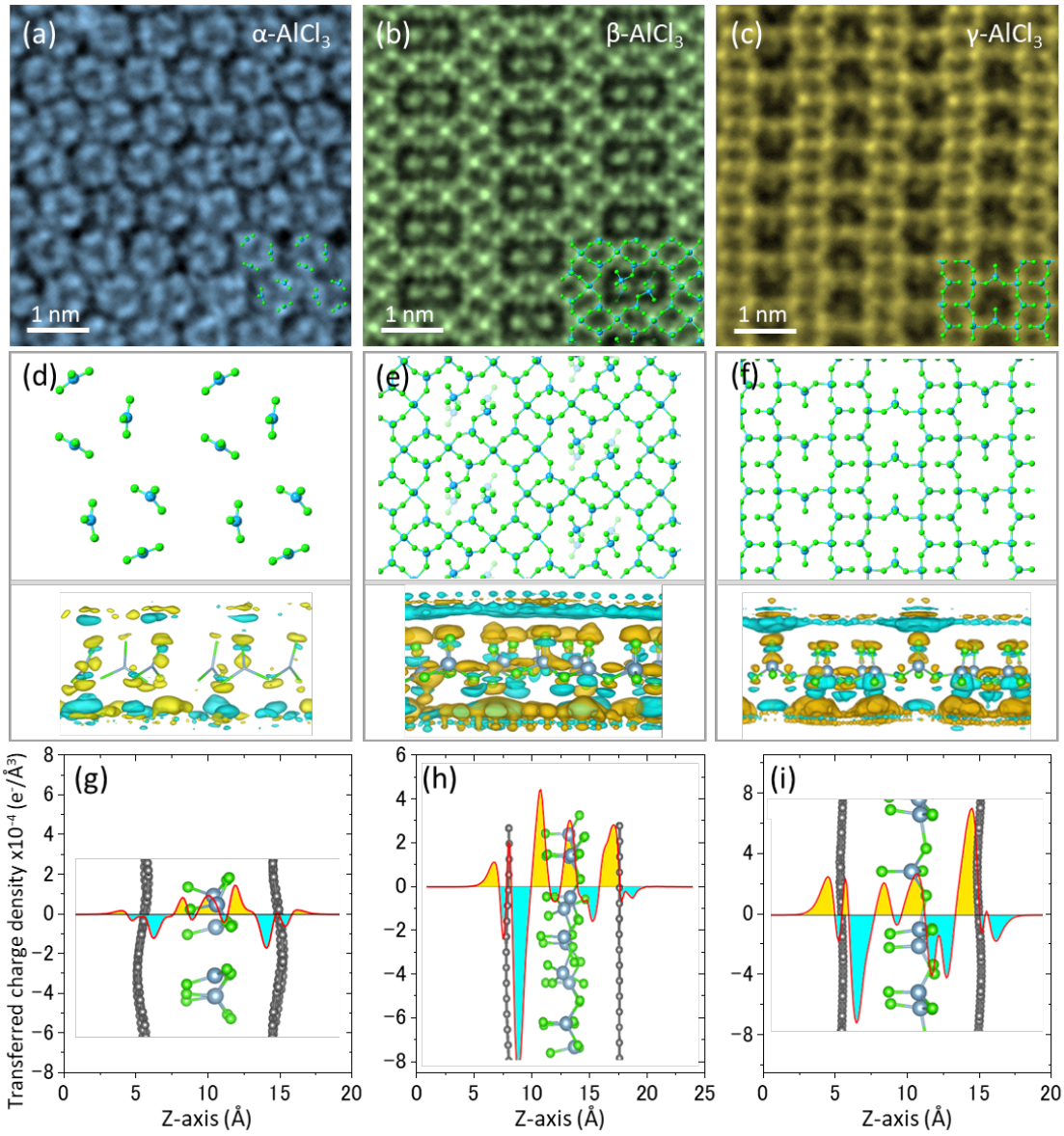

Fig. 2. Polymorphic phases of 2D-$AlCl_3$. (a–c) ADF images of the three different phases of 2D-$AlCl_3$ (α, β, and γ). (d–f) Corresponding 2D-$AlCl_3$ atomic models with top and side view. DFT-calculated electron transfer isosurfaces are superimposed on the side views of corresponding models. The two $AlCl_3$ units in the β-$AlCl_3$ "eye mask" cage have two meta stable configurations allowing for translational swap. The isosurface value is set to

1.3×10^{-4} e/Å^3, and the yellow and cyan areas represent an excess and depletion of electrons, respectively. (g–i) Charge density difference averaged in the *x*-*y* plane vs. the *z*-coordinate.

After analyzing the polymorphic phases of $AlCl_3$, which included the newly discovered phases, their phase transformations under the electron beam were examined by *in situ* STEM. Figure 3a–3d shows consecutive ADF images of a large-area phase transformation of α-$AlCl_3$ to β-$AlCl_3$ (see Movie 1). The entire scanning area of the α-$AlCl_3$ phase (8 × 8 nm^2) transforms into the β-$AlCl_3$ phase within 3 min. This transformation is irreversible under e-beam irradiation, which suggests that β-$AlCl_3$ is a chlorine-deficient phase ($AlCl_{3-x}$, Al_6Cl_{17} from the DFT calculations). During e-beam scanning, the α-$AlCl_3$ phase begins to reassemble its structure to form rhombus-shaped octagons, and a combination of octagons constructs the framework surrounding the eye-mask-shaped icositetragons of the β-$AlCl_3$ phase, as shown in Fig. S4. Figure 3e shows a comparison of the formation energies of the 2D-$AlCl_3$ phases. The calculations indicate that they are metastable, with a higher (negatively defined) energy than that of *n*-$AlCl_3$ by 0.12–0.23 eV/atom (Table S3). Among them, α-$AlCl_3$ has a highest formation energy and tends to transform into the relatively stable β-$AlCl_3$ phase. Notably, the α-to-γ-$AlCl_3$ phase transformation was not observed in the *in situ* STEM experiment. The β-$AlCl_3$ and γ-$AlCl_3$ phases possess geometrically similar structures with comparable formation energies, and the γ-$AlCl_3$ phase is also chlorine-deficient (Al_5Cl_{14} from the DFT calculations). These two phases share the rhombus-shaped octagon rows to form seamless domain boundaries as shown in Fig. S5. All these 2D-$AlCl_3$ structures were found to be

present and even co-exist, as evident from the low-magnification STEM images in Fig. S6. The newly discovered α-, β-, and γ-$AlCl_3$ structures have never been found as the bulk crystals. The most energetically stable phase is *n*-$AlCl_3$, but we never see any structural transformation from α-, β-, and γ-$AlCl_3$ to *n*-$AlCl_3$ during the STEM observation. So, we infer that the α-, β-, and γ-phases are thermodynamically (meta-)stable with the existence of BLG and the BLG may prevent them to transform to the most stable *n*-$AlCl_3$ phase. Discussions about the different DFT levels and lattice dynamic stability of the 2D phases are made in supplementary information (Fig. S7).

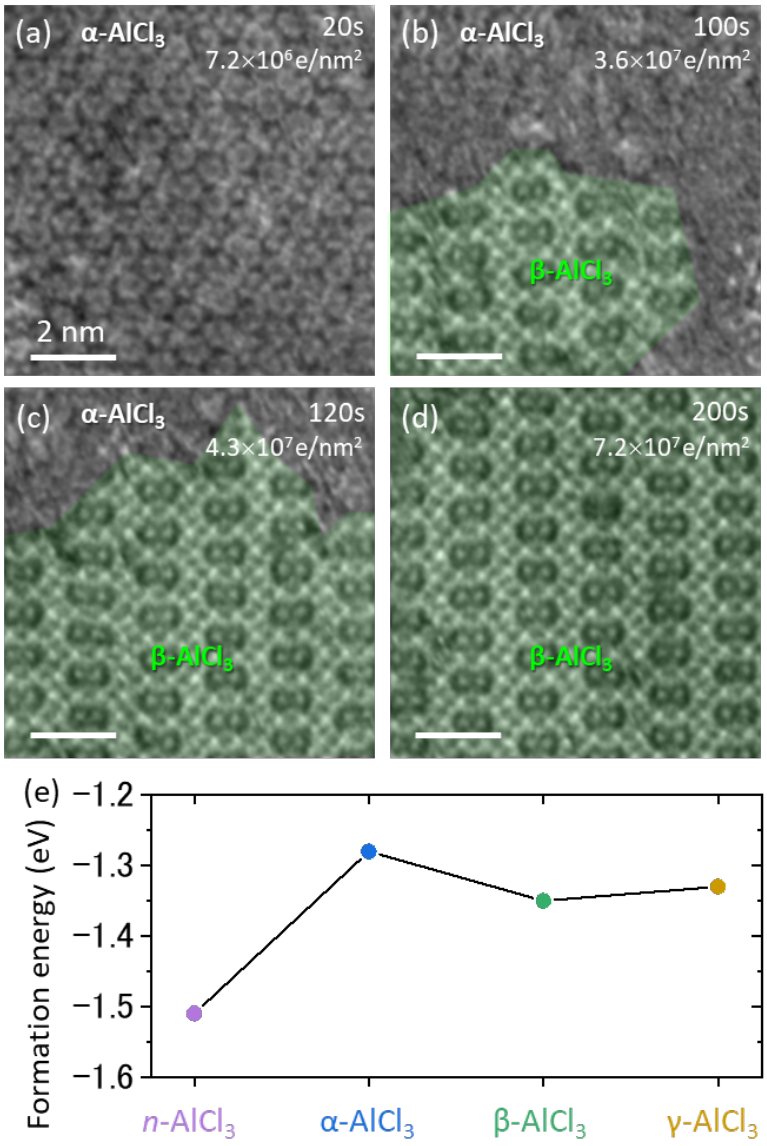

Fig. 3. Phase transformations of 2D-$AlCl_3$. (a–d) Consecutive ADF images of the phase transformation of α-$AlCl_3$ to β-$AlCl_3$ (green-colored regions). (e) Comparison of the formation energies of the four 2D-$AlCl_3$ phases.

$CuCl_2$ is one of the commonly used ingredients for hybrid intercalation to assist the intercalation of other MCl_x by providing chlorine gas during the chemical vapor transport

growth process[45]. Figure 4a shows an ADF image of $CuCl_2$@BLG. The 2D-$CuCl_2$ compound exhibits trigonal symmetry and consists of long parallel $CuCl_2$ chains, as shown by the atomic model in the inset of Fig. 4a. This structure is different from the standard octahedral (1T) structure of MCl_2 (Fig. 1b). Interestingly, 2D-$CuCl_2$ was found to locally transform its structure into one with distorted octahedral symmetry (T'-$CuCl_2$) without parallel chains, as shown in Fig. S8 and Movie 2. DFT calculations indicated that both structures are stable, with the T' phase being higher in energy by ~0.12 eV per formula unit (Fig. S9). Electrons appear to be transferred from BLG to 2D-$CuCl_2$ (Fig. 4b, 4c). A significantly higher density of electrons transferred to graphene 4.6×10^{13} e/cm^2 (Table S2) was obtained from Bader analysis and integration of the electron densities compared to that of $AlCl_3$.

Composite structures can be created when several elements are simultaneously intercalated between the BLG gaps. Figure 4D shows an ADF image of an area with co-existing $AlCl_3$ and $CuCl_2$. This structure can be referred to as a heterogeneous mixture (ordered alloy) in a seamless in-plane quasi-1D γ-$AlCl_3$/$CuCl_2$. An EELS line scan was performed along the yellow line shown in Fig. 4d, and the corresponding EELS 2D profile in the energy range of 900–960 eV is shown in Fig. 4E. The appearance of Cu L_3-edge white lines at 930 eV hints at the locations of $CuCl_2$ chains, which are indicated by red triangles; the subsequent loading of the interstitial spaces with $AlCl_3$ is also confirmed (EELS profiles in Fig. S3). The interstitial $AlCl_3$ is composed of the γ-$AlCl_3$ phase, which forms a crystalline structure in the sufficiently wide space between two $CuCl_2$ lines; otherwise, it can only exist as a partial crystalline structure in a narrow space. Another type of $AlCl_3$/$CuCl_2$ alloy, a mixture of α-$AlCl_3$ and $CuCl_2$, features islands of $CuCl_2$ separated by α-$AlCl_3$ domains with a more disordered arrangement, as shown in Fig. S10.

The co-doping mechanism of $AlCl_x$ and $CuCl_x$ is assumed to involve the intercalation of $CuCl_2$ and subsequent replacement by $AlCl_3$[45], or mixing of Cu and Al in the gas phase where $CuAl_2Cl_8$ is considered as a complex species in the co-intercalation[46–48]. Complete mixing of Al and Cu atoms was not clearly observed via STEM in the present study; this presumably indicates that the intercalation occurs primarily with $AlCl_3$ and $CuCl_2$ vapors, or $CuAl_2Cl_8$ possibly dissociates during diffusion in the 2D nanospace. Numerous studies on GICs have been attempted for a long time by employing effective techniques to directly visualize the local atomic arrangements of specimens for precisely correlating the macroscopic measurements of the properties to the real atomic structures. Various domains of Al and Cu as well as their mixed phases, but not a unique homogeneous structure, are clearly shown herein by utilizing large-area BLG. The obtained STEM results of intercalated polymorphic phases provide a novel strategy for developing a doping mechanism for co-intercalation.

EELS profiles in the low-energy range (0.2–1.5 eV) were subsequently collected using a monochromatic electron source to detect the charge carrier plasmon, as shown in Fig. 4f. The *n*-, α-, β-$AlCl_3$ phases exhibits a single peak at 0.70, 0.69, and 0.72 eV, respectively. The γ-$AlCl_3$ phase exhibits a broader peak at a lower energy of 0.65 eV. The $CuCl_2$ domain shows a peak at a higher energy (0.77 eV), and the γ-$AlCl_3$/$CuCl_2$ alloy essentially combines the charge carrier plasmon features of these two materials. The plasma angular frequency can be expressed using the Drude model as follows:

$$\omega_p = \sqrt{\frac{ne^2}{\varepsilon_0 m^*}},$$

where n, e, ε_0, and m^* represent the carrier density, electron charge, the permittivity of free space, and effective mass of electrons, respectively. The charge carrier density

transferred from graphene to each phase of the 2D-$AlCl_3$ and 2D-$CuCl_2$ compounds can be further derived; values of 1.07–1.5 × 10^{13} cm^{-2} are obtained using the Drude model and vdW gap of 3.5 Å (Table S2). The charge carrier plasmon energy is known to shift to lower energies with decreasing electron densities, assuming electron transfer from graphene to the intercalants[49–51].

The intercalation of $AlCl_3$ and $CuCl_2$ in BLG represents p-type doping, which is in overall agreement with the DFT calculations (Figs. S11–15) and a cross-checked using a more advanced Tkatchenko-Scheffler (TS) dispersion correction method comprising the iterative Hirshfeld partitioning scheme (Fig. S16). Macroscopic measurements for the metallic/semiconducting behaviors of each phase are not easy because the two graphene layers on the surface prevent the typical 4-probe measurements. Upon the intercalation of $AlCl_3$ and $CuCl_2$, BLG exhibits a Raman G-band shift from 1585 cm^{-1} to 1610–1620 cm^{-1} (Fig. S17) and the carrier density can be estimated as ~3 × 10^{13} cm^{-2}[52], which is consistent with the value derived using the Drude model and the DFT calculation results. The calculations indicate that the γ phase of intercalated $AlCl_3$ is a semimetal, the β phase is a semiconductor, and the molecular α–phase has insulating properties. All phases of $CuCl_2$ are insulators. The elucidation of charge-related transformations of structures is crucial in the context of various energy-storage-related applications and the further development of electronic devices[38,45,53–58].

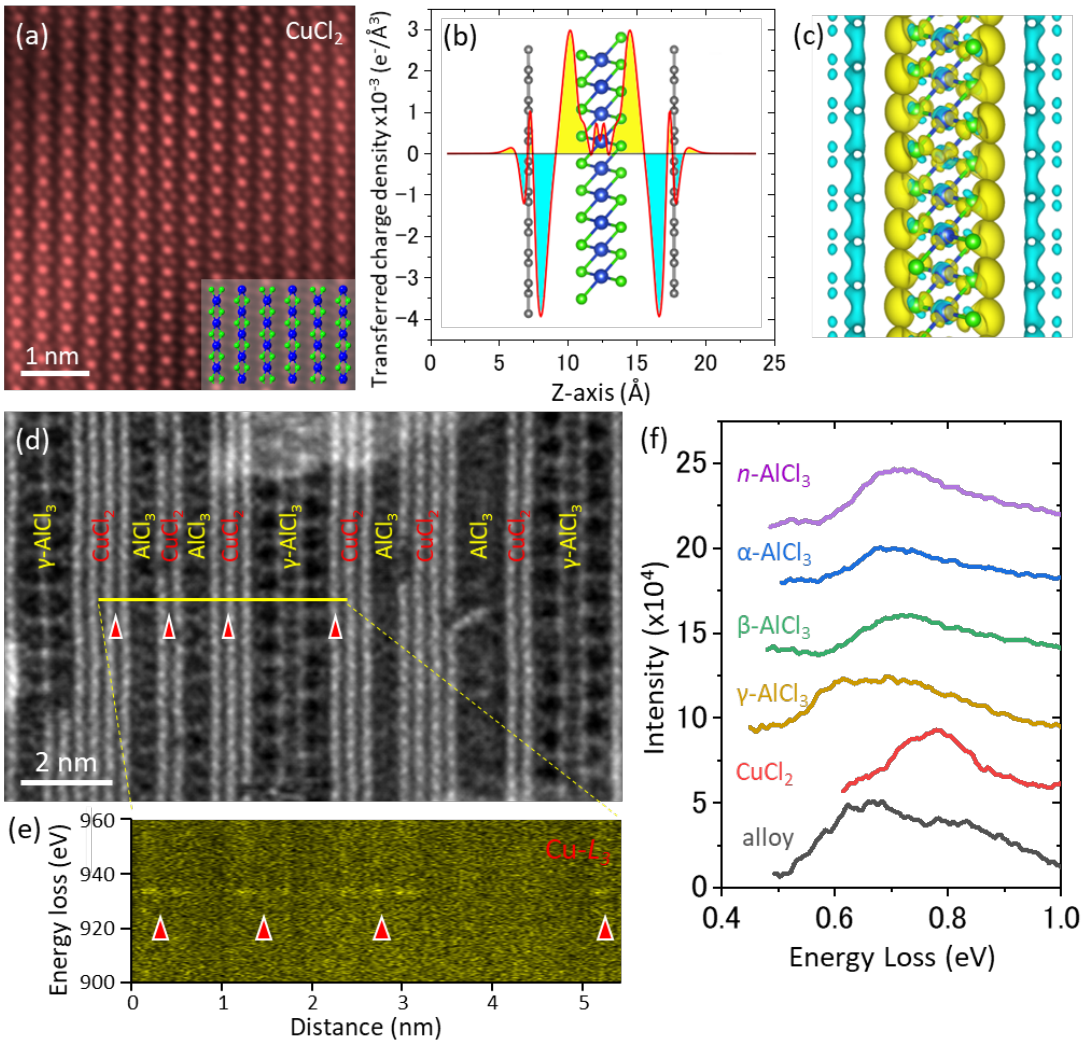

Fig. 4. Optical properties of the $AlCl_3$ and $CuCl_2$ phases and their alloy. (a) ADF image of $CuCl_2$ intercalated in BLG. (b) Charge density difference plot of BLG and $CuCl_2$ averaged in the *x*-*y* plane vs. the *z*-coordinate. (c) DFT-calculated electron transfer isosurfaces superimposed on the side view of the model. The isosurface value is set to be 6×10^{-4} e/Å^3, and the yellow and cyan areas represent electron excess and depletion, respectively. (d) ADF image of the γ-$AlCl_3$/$CuCl_2$ 2D alloy. $CuCl_2$ chains are indicated by red triangles. (e) EELS 2D profile scanned along the yellow line shown in (d), where the presence of the Cu *L*-edge is indicated by red triangles. (f) EELS low-loss profiles showing charge carrier plasmon peaks of the 2D-$AlCl_3$ phases, $CuCl_2$, and the alloy.

This study may have a significant impact on the understanding of GICs and the growth of 2D materials in vdW gaps. The atomic arrangement of 2D metal chlorides in the vdW gaps of BLG has been unveiled herein, which could be the key to answering the fundamental questions on the property/structure relationships of GICs that have been unresolved, in spite of a century-long research of these systems. The structural transformations of intercalated materials and the correlated charge transfer between the graphite layers are crucial for a better understanding of electrical conductivity and battery characteristics. Polymorphic phase transitions that may exist in vdW gaps must be considered because simple GIC models typically fail to explain the properties of GICs. The *in situ* observation of phase-transformation-related charge transfer in the GICs herein mimics the electrochemical reactions and deepens the understanding of the process of intercalation. Furthermore, multiple-compound intercalation offers infinite possibilities for the development of various novel intercalated 2D structures with unique characteristics, and a plethora of intriguing physics and chemistry can therefore be subsequently explored in 2D nanospaces.

Method

Material growth

A uniform BLG sheet was synthesized by ambient-pressure chemical vapor deposition (CVD) using a Cu–Ni alloy thin film that was deposited on c-plane sapphire, as reported previously[36]. The BLG sheet was transferred onto a TEM grid by etching the Cu–Ni film

with an etching solution (aqueous solution of ammonium persulfate), followed by thorough washing with pure water.

For co-intercalation, a method similar to that used for the intercalation of $MoCl_5$ in BLG was employed[38]. BLG supported on a TEM grid was sealed in a Pyrex tube with $FeCl_3$, $AlCl_3$ and $CuCl_2$ powders after evacuating the tube at ~5×10^{-4} Pa for 1 h. The weight ratio of the $AlCl_3$ and $CuCl_2$ intercalants was set to be 2:1. Co-intercalation was performed by heating both the BLG and the metal chlorides at 150 °C for 30 min. The $FeCl_3$ intercalation was performed by heating at 250 °C for 1 hr. The Pyrex tube was opened in a glove box, and the sample was placed on a JEOL vacuum transfer holder and then transferred to the TEM chamber immediately to avoid possible degradation under ambient conditions.

STEM and EELS

STEM images were acquired using an ultra-high vacuum ARM200F-based microscope equipped with a JEOL delta corrector and a cold field emission gun operating at 60 kV. A probe current of ~15–20 pA, and a convergence semi-angle and inner acquisition semi-angle of 37 mrad and 76 mrad, respectively, were used. A typical ADF image was 1024 × 1024 pixels in resolution and captured using a pixel time of 38.5 μs. The EELS core-loss profiles were recorded using a Gatan Rio CMOS camera optimized for low-voltage operation. EELS profiles were acquired using line scans with an exposure time of 0.1 s/pixel. The EELS low-loss profiles were recorded using a delta-type aberration-corrected JEM-ARM200F system equipped with a Schottky field-emission gun operating at 60 kV and a double Wien-filter monochromator. A convergence semi-angle of 43 mrad and an

inner acquisition semi-angle of 125 mrad were used. A Gatan Quantum-ERS camera optimized at low-voltages was used for high-resolution EELS. The beam current was 8.1 pA with an energy resolution of 45 meV after inserting a 0.5 μm slit. All STEM images and EELS profiles were recorded at room temperature. Gaussian Blur filter is applied to the STEM images by using ImageJ.

Density functional theory calculations

Spin-polarized simulations were performed using the Vienna ab-initio Simulation Package (VASP)[59,60]. The structures were relaxed using the Perdew–Burke–Ernzerhof (PBE) exchange-correlation functional[61] with a force tolerance of 0.01 eV/Å (electronic convergence criteria of 10^{-5} eV). The energy cut-off was set to 400 eV, and a 5×5×1 k-points using Brillouin zone integration with the tetrahedron method and Blöchl corrections. Van-der-Waals interactions are taken into account using the DFT-D3 method[62] with Becke-Jonson damping. The structures of the selected phases were also investigated using a more advanced Tkatchenko-Scheffler (TS) dispersion correction method[63] comprising the iterative Hirshfeld partitioning scheme.

The 2D structures were initially relaxed without the bilayer graphene (BLG) which was con-secutively introduced with minimal strain (<1%) imposed on the BLG. Their stability was then checked including the BLG encapsulation. The obtained relaxed structures are included in the supplementary information.

Charge transfer between graphene and the intercalated materials was assessed by: (i) calculating the charge difference between the combined system and isolated components and subsequently integrating over the corresponding areas, and (ii) using Bader analysis. Details of the charge transfer calculations can be found elsewhere [20].

Acknowledgement

Y.-C.L. and K.S. acknowledge JSPS-KAKENHI [(JP16H06333), (18K14119)], the JST-CREST program (JPMJCR20B1, JMJCR20B5, JPMJCR1993), the JSPS A3 Foresight Program, and the Kazato Research Encouragement Prize. HA acknowledges JSPS-KAKENHI (18H03864 and 19K22113) and the JST-CREST program (JPMJCR20B1). AVK thanks the German Research Foundation (DFG; project KR 4866/2-1) for support. We thank HRLS Stuttgart, Germany, TU Dresden (Taurus cluster), and CSC Finland for generously providing computing time. We acknowledge Dr. Pablo Solís-Fernández and Prof. Rika Matsumoto for providing high-quality BLG and facilitating valuable discussions.

Reference

[1] Y. Liu, Y. Huang, X. Duan, *Nature* **2019**, *567*, 323.

[2] Y. Gong, J. Lin, X. Wang, G. Shi, S. Lei, Z. Lin, X. Zou, G. Ye, R. Vajtai, B. I. Yakobson, H. Terrones, M. Terrones, B. K. Tay, J. Lou, S. T. Pantelides, Z. Liu, W. Zhou, P. M. Ajayan, *Nat. Mater.* **2014**, *13*, 1135.

[3] K. S. Novoselov, A. Mishchenko, A. Carvalho, A. H. Castro Neto, *Science* **2016**, *353*, acc9439.

[4] M. P. Levendorf, C. J. Kim, L. Brown, P. Y. Huang, R. W. Havener, D. A. Muller, J. Park, *Nature* **2012**, *488*, 627.

[5] C. Huang, S. Wu, A. M. Sanchez, J. J. P. Peters, R. Beanland, J. S. Ross, P. Rivera, W. Yao, D. H. Cobden, X. Xu, *Nat. Mater.* **2014**, *13*, 1096.

[6] Z. Zhang, P. Chen, X. Duan, K. Zang, J. Luo, X. Duan, *Science* **2017**, *357*, 799.

[7] P. K. Sahoo, S. Memaran, Y. Xin, L. Balicas, H. R. Gutiérrez, *Nature* **2018**, *553*, 63.

[8] J. Li, X. Yang, Y. Liu, B. Huang, R. Wu, Z. Zhang, B. Zhao, H. Ma, W. Dang, Z. Wei, K. Wang, Z. Lin, X. Yan, M. Sun, B. Li, X. Pan, J. Luo, G. Zhang, Y. Liu, Y. Huang, X. Duan, X. Duan, *Nature* **2020**, *579*, 368.

[9] R. Xiang, T. Inoue, Y. Zheng, A. Kumamoto, Y. Qian, Y. Sato, M. Liu, D. Tang, D. Gokhale, J. Guo, K. Hisama, S. Yotsumoto, T. Ogamoto, H. Arai, Y. Kobayashi, H. Zhang, B. Hou, A. Anisimov, M. Maruyama, Y. Miyata, S. Okada, S. Chiashi, Y. Li, J. Kong, E. I. Kauppinen, Y. Ikuhara, K. Suenaga, S. Maruyama, *Science* **2020**, *367*, 537.

[10] H. Yoo, R. Engelke, S. Carr, S. Fang, K. Zhang, P. Cazeaux, S. H. Sung, R. Hovden, A. W. Tsen, T. Taniguchi, K. Watanabe, G. C. Yi, M. Kim, M. Luskin, E. B. Tadmor, E. Kaxiras, P. Kim, *Nat. Mater.* **2019**, *18*, 448.

[11] Y. Cao, V. Fatemi, S. Fang, K. Watanabe, T. Taniguchi, E. Kaxiras, P. Jarillo-Herrero, *Nature* **2018**, *556*, 43.

[12] T. H. Bointon, I. Khrapach, R. Yakimova, A. V. Shytov, M. F. Craciun, S. Russo, *Nano Lett.* **2014**, *14*, 1751.

[13] N. Kim, K. S. Kim, N. Jung, L. Brus, P. Kim, *Nano Lett.* **2011**, *11*, 860.

[14] S. Xie, L. Tu, Y. Han, L. Huang, K. Kang, K. U. Lao, P. Poddar, C. Park, D. A. Muller, R. A. DiStasio, J. Park, *Science* **2018**, *359*, 1131.

[15] P. K. Gogoi, Y.-C. Lin, R. Senga, H.-P. Komsa, S. L. Wong, D. Chi, A. V. Krasheninnikov, L.-J. Li, M. B. H. Breese, S. J. Pennycook, A. T. S. Wee, K. Suenaga, *ACS Nano* **2019**, *13*, 9541.

[16] K. Suenaga, T. Tence, C. Mory, C. Colliex, H. Kato, T. Okazaki, H. Shinohara, K. Hirahara, S. Bandow, S. Iijima, *Science* **2000**, *290*, 2280.

[17] M. S. Dresselhaus, G. Dresselhaus, *Adv. Phys.* **1981**, *30*, 139.

[18] J. Wan, S. D. Lacey, J. Dai, W. Bao, M. S. Fuhrer, L. Hu, *Chem. Soc. Rev.* **2016**, *45*, 6742.

[19] X. Zhao, P. Song, C. Wang, A. C. Riis-Jensen, W. Fu, Y. Deng, D. Wan, L. Kang, S. Ning, J. Dan, T. Venkatesan, Z. Liu, W. Zhou, K. S. Thygesen, X. Luo, S. J. Pennycook, K. P. Loh, *Nature* **2020**, *581*, 171.

[20] I. V. Chepkasov, M. Ghorbani-Asl, Z. I. Popov, J. H. Smet, A. V. Krasheninnikov, *Nano Energy* **2020**, *75*, 104927.

[21] K. Fredenhagen, G. Cadenbach, *Zeitschrift für Anorg. und Allg. Chemie* **1926**, *158*, 249.

[22] G. R. Hennig, *Prog. Inorg. Chem.* **1959**, *1*, 125.

[23] R. C. Croft, *Aust. J. Chem.* **1956**, *9*, 184.

[24] A. Manthiram, C. Tsang, *Adv. Mater.* **1998**, *10*, 265.

[25] J. Xu, Y. Dou, Z. Wei, J. Ma, Y. Deng, Y. Li, H. Liu, S. Dou, *Adv. Sci.* **2017**, *4*, 1700146.

[26] N. B. Hannay, T. H. Geballe, B. T. Matthias, K. Andres, P. Schmidt, D. MacNair, *Phys. Rev. Lett.* **1965**, *14*, 225.

[27] N. Emery, C. Hérold, M. D'Astuto, V. Garcia, C. Bellin, J. F. Marêché, P. Lagrange, G. Loupias, *Phys. Rev. Lett.* **2005**, *95*, 087003.

[28] T. E. Weller, M. Ellerb, S. S. Saxena, R. P. Smith, N. T. Skipper, *Nat. Phys.* **2005**, *1*, 39.

[29] K. Kanetani, K. Sugawara, T. Sato, R. Shimizu, K. Iwaya, T. Hitosugi, T.

Takahashi, *Proc. Natl. Acad. Sci. U. S. A.* **2012**, *109*, 19610.

[30] I. Khrapach, F. Withers, T. H. Bointon, D. K. Polyushkin, W. L. Barnes, S. Russo, M. F. Craciun, *Adv. Mater.* **2012**, *24*, 2844.

[31] T. H. Bointon, S. Russo, M. F. Craciun, *IET Circuits, Devices Syst.* **2015**, *9*, 403.

[32] M. C. Lin, M. Gong, B. Lu, Y. Wu, D. Y. Wang, M. Guan, M. Angell, C. Chen, J. Yang, B. J. Hwang, H. Dai, *Nature* **2015**, *520*, 325.

[33] M. Angell, C. J. Pan, Y. Rong, C. Yuan, M. C. Lin, B. J. Hwang, H. Dai, *Proc. Natl. Acad. Sci. U. S. A.* **2017**, *114*, 834.

[34] M. Kühne, F. Börrnert, S. Fecher, M. Ghorbani-Asl, J. Biskupek, D. Samuelis, A. V. Krasheninnikov, U. Kaiser, J. H. Smet, *Nature* **2018**, *564*, 234.

[35] J. P. Bonacum, A. O'Hara, D. L. Bao, O. S. Ovchinnikov, Y. F. Zhang, G. Gordeev, S. Arora, S. Reich, J. C. Idrobo, R. F. Haglund, S. T. Pantelides, K. I. Bolotin, *Phys. Rev. Mater.* **2019**, *3*, 064004.

[36] Y. Takesaki, K. Kawahara, H. Hibino, S. Okada, M. Tsuji, H. Ago, *Chem. Mater.* **2016**, *28*, 4583.

[37] P. Solís-Fernández, Y. Terao, K. Kawahara, W. Nishiyama, T. Uwanno, Y.-C. Lin, K. Yamamoto, H. Nakashima, K. Nagashio, H. Hibino, K. Suenaga, H. Ago, *ACS Nano* **2020**, *14*, 6834.

[38] H. Kinoshita, I. Jeon, M. Maruyama, K. Kawahara, Y. Terao, D. Ding, R. Matsumoto, Y. Matsuo, S. Okada, H. Ago, *Adv. Mater.* **2017**, *29*, 1702141.

[39] K. Ohashi, I. Tsujikawa, *Tanso* **1978**, *95*, 154.

[40] R. Senga, H.-P. Komsa, Z. Liu, K. Hirose-Takai, A. V Krasheninnikov, K. Suenaga, *Nat. Mater.* **2014**, *13*, 1050.

[41] T. Pham, S. Oh, P. Stetz, S. Onishi, C. Kisielowski, *Science* **2018**, *361*, 263.

[42] H. Shinohara, *Reports Prog. Phys.* **2000**, *63*, 843.

[43] G. A. Botton, C. J. Humphreys, *Micron* **1997**, *28*, 313.

[44] T. Malis, S. C. Cheng, R. F. Egerton, *J. Electron Microsc. Tech.* **1988**, *8*, 193.

[45] R. Matsumoto, Y. Okabe, *Synth. Met.* **2016**, *222*, 351.

[46] D. E. Wessbecher, W. C. Forsman, *Synth. Met.* **1991**, *40*, 219.

[47] M. Inagaki, M. Ohira, *Tanso* **1993**, *159*, 222.

[48] F. P. Emmenegger, *Inorg. Chem.* **1977**, *16*, 343.

[49] J. Lin, J. Yuan, K. Jin, Z. Yin, G. Li, K. J. Zhou, X. Lu, M. Dantz, T. Schmitt, H. Ding, H. Guo, M. P. M. Dean, X. Liu, *npj Quantum Mater.* **2020**, *5*, 1.

[50] S. Y. Shin, N. D. Kim, J. G. Kim, K. S. Kim, D. Y. Noh, K. S. Kim, J. W. Chung, *Appl. Phys. Lett.* **2011**, *99*, 082110.

[51] C. Kramberger, F. Roth, R. Schuster, R. Kraus, M. Knupfer, E. Einarsson, S. Maruyama, D. J. Mowbray, A. Rubio, T. Pichler, *Phys. Rev. B* **2012**, *85*, 085424.

[52] A. Das, S. Pisana, B. Chakraborty, S. Piscanec, S. K. Saha, U. V. Waghmare, K. S. Novoselov, H. R. Krishnamurthy, A. K. Geim, A. C. Ferrari, A. K. Sood, *Nat. Nanotechnol.* **2008**, *3*, 210.

[53] D. Zhan, L. Sun, Z. H. Ni, L. Liu, X. F. Fan, Y. Wang, T. Yu, Y. M. Lam, W. Huang, Z. X. Shen, *Adv. Funct. Mater.* **2010**, *20*, 3504.

[54] Y. Li, Y. Lu, P. Adelhelm, M. M. Titirici, Y. S. Hu, *Chem. Soc. Rev.* **2019**, *48*, 4655.

[55] J. Zhou, Z. Lin, H. Ren, X. Duan, I. Shakir, Y. Huang, X. Duan, **2021**, *2004557*, 1.

[56] J. W. Yang, G. Lee, J. S. Kim, K. S. Kim, *J. Phys. Chem. Lett.* **2011**, *2*, 2577.

[57] J. Nathaniel, X. Q. Wang, *Appl. Phys. Lett.* **2012**, *100*, 213112.

[58] D. Kondo, H. Nakano, B. Zhou, I. Kubota, K. Hayashi, K. Yagi, M. Takahashi, M. Sato, S. Sato, N. Yokoyama, in *Proc. 2013 IEEE Int. Interconnect Technol. Conf. IITC 2013*, **2013**.

[59] G. Kresse, J. Furthmüller, *Phys. Rev. B* **1996**, *54*, 11169.

[60] G. Kresse, D. Joubert, *Phys. Rev. B* **1999**, *59*, 1758.

[61] J. P. Perdew, K. Burke, M. Ernzerhof, *Phys. Rev. Lett.* **1996**, *77*, 3865.

[62] S. Grimme, J. Antony, S. Ehrlich, H. Krieg, *J. Chem. Phys.* **2010**, *132*, 154104.

[63] A. Tkatchenko, M. Scheffler, *Phys. Rev. Lett.* **2009**, *102*, 073005.